Relating Interactions between Neurofilaments to the Structure of Axonal Neurofilament Distributions through Polymer Brush Models

Sanjay Kumar,* Xinghua Yin,† Bruce D. Trapp,† Jan H. Hoh,*‡ and Michael E. Paulaitis‡

*Department of Physiology, Johns Hopkins University School of Medicine, Baltimore, Maryland 21205; †Department of Neurosciences, Lerner Research Institute, Cleveland Clinic Foundation, Cleveland, Ohio 44195; and ‡Department of Chemical Engineering, Johns Hopkins University, Baltimore, Maryland 21218 USA

ABSTRACT Neurofilaments (NFs) have been proposed to interact with one another through mutual steric exclusion of their unstructured C-terminal "sidearm" domains, producing order in axonal NF distributions and conferring mechanical strength to the axon. Here we apply theory developed for polymer brushes to examine the relationship between the brush properties of the sidearms and NF organization in axons. We first measure NF–NF radial distribution functions and occupancy probability distributions for adult mice. Interpreting the probability distributions using information theory, we show that the NF distributions may be represented by a single pair potential of mean force. Then, to explore the relationship between model parameters and NF architecture, we conduct two-dimensional Monte Carlo simulations of NF cross-sectional distributions. We impose purely repulsive interaction potentials in which the sidearms are represented as neutral and polyelectrolyte chains. By treating the NFs as telechelic polymer brushes, we also incorporate cross-bridging interactions. Both repulsive potentials are capable of reproducing NF cross-sectional densities and their pair correlations. We find that NF structure is sensitive to changes in brush thickness mediated by chain charge, consistent with the experimental observation that sidearm phosphorylation regulates interfilament spacing. The presence of attractive cross-bridging interactions contributes only modestly to structure for moderate degrees of cross-bridging and leads to NF aggregation for extensive cross-bridging.

INTRODUCTION

Neurofilaments (NFs) comprise an abundant and functionally important cytoskeletal component of large, myelinated neurons. These intermediate filaments run in parallel along the axon and occupy a large fraction of the axoplasmic volume. When the axon is cut in cross section, the transected NFs appear as a two-dimensional distribution of punctate structures with liquid-like order (Fig. 1, *A* and *B*). The observation that NFs are spaced at nonrandom distances in the axon suggests that the NFs interact with one another (Hsieh et al., 1994). Through these interactions, axonal NFs generate an ordered intracellular framework that maintains and protects axonal patency and buttresses the axon against external compressive stresses. Evidence for the importance of NFs to the mechanical properties of axons comes from structural and mechanical studies on isolated axons (McHale et al., 1995; Povlishock and Christman, 1995; Smith et al., 1999) and rheological measurements on purified NF gels (Leterrier and Eyer, 1987; Gou et al., 1998). Intracellular NF aggregation is also a central finding in several neurodegenerative diseases (e.g., amyotrophic lateral sclerosis, Parkinson's Disease), suggesting that altered interactions between NFs may participate in the pathological process (Julien, 1999).

Submitted November 1, 2001 and accepted for publication January 18, 2002.

Address reprint requests to Michael E. Paulaitis, Dept. of Chemical Engineering, Johns Hopkins University, 221 Maryland Hall, 3400 N. Charles St., Baltimore, MD 21218. Tel.: 410-516-7170; Fax: 410-516-5510; E-mail: michaelp@jhu.edu.

0006-3495/02/05/2360/13 $2.00

Mammalian NFs are composed of three polypeptide subunits: light (NF-L, 61 kDa in humans), medium (NF-M, 90 kDa), and heavy (NF-H, 110 kDa) (Lee and Cleveland, 1996). The amino terminus of each subunit contains a rod domain of ~300 residues in length, which associates with the rod domains of the other subunits to form the filament "backbone." The amino terminus of each subunit also contains a head domain of ~100 residues, which, together, are thought to facilitate end-to-end association of heterotrimers to form complete filaments. The carboxy terminus of NF-M and NF-H each contains a long tail domain of more than 300 and 600 residues, respectively, which protrudes from the backbone to form the NF "sidearms." Electron microscopy (EM) of isolated NFs reveals that these sidearms extend 75–100 nm from the filament backbone (Geisler and Weber, 1981). Thus, the assembled NF has a cylindrical core–shell structure in which the core is formed by the filament backbone and the shell is formed by the extended sidearms (Fig. 1 *C*). These sidearms are believed to mediate interactions between the filaments.

Several distinct models have been proposed for NF–NF interactions that lead to axonal NF structure. In one model, the sidearms interact through binding or cross-bridging interactions, mediated by the sidearms themselves or by accessory factors. Support for this model comes from EM studies of axonal (Hisanaga and Hirokawa, 1988), and purified (Chen et al., 2000) NF distributions, and rheological data (Gou et al., 1998). No cross-linking agent has yet been identified; neuronal bullous pemphigoid antigen 1 (BPAG1n) was found to cross-link NFs to the actin cytoskeleton (Yang et al., 1996), although this finding was contradicted by a subsequent report (Leung et al., 1999). In

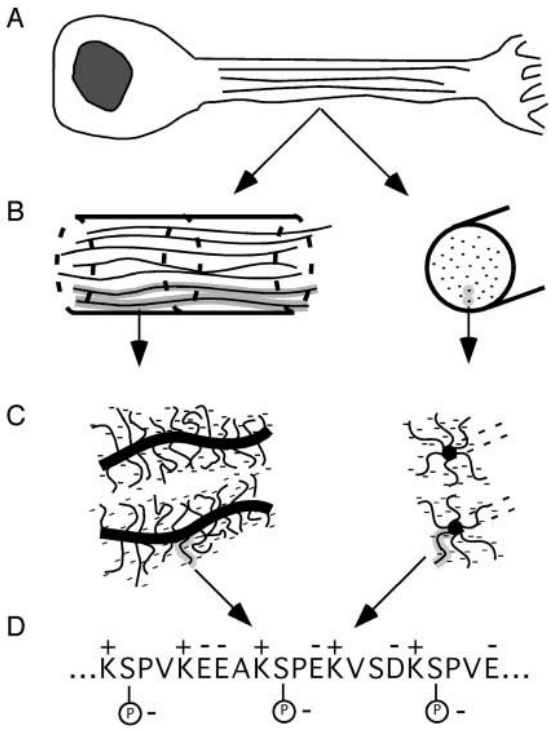

FIGURE 1 Organization of axonal neurofilaments. (*A*) NFs run in parallel along the length of the axon. (*B*) In cross section, the NF cores appear as particulate features with two-dimensional structure. (*C*) Individually, NFs have a core–shell structure, in which the core is formed by the backbone of the three subunit amino termini and the shell is formed by the carboxy terminal sidearms of NF-H and NF-M. (*D*) Charge from the constituent amino acids is locally high but globally near-neutral. Extensive phosphorylation produces significant net negative charge.

a second model, the filaments repel one another through direct, colloidal electrostatic forces. Here, the net negative charge on the sidearms is acquired through extensive phosphorylation (Fig. 1 *D*). This model is supported by an observed correlation between NF phosphorylation and mean interfilament spacing in vivo (de Waegh et al., 1992; Strong et al., 2001). Also, purified NF gel properties depend strongly on phosphorylation levels (Eyer and Leterrier, 1988). In the third and most recently-proposed model, the sidearms are unstructured polyelectrolyte chains, forming a hairy, polymer brush-like layer around the filament backbone. Interfilament repulsion is achieved through mutual steric exclusion by the sidearms; i.e., the sidearms function as a so-called "polymer brush." Here, electrostatic repulsion operates on a far shorter range, governing brush structure through monomer–monomer repulsion. Evidence for this model comes primarily from atomic force microscopy (AFM), in which exclusion of small particles from the filament backbone was observed, and in which repulsive forces extending up to 50 nm from the filament backbone were detected, even in high-salt buffer (Brown and Hoh, 1997; Hoh, 1998). Support for similar mechanisms has now been gathered in several other systems, including stabilization of microtubules by microtubule-associated proteins (Mukhopadhyay and Hoh, 2001) and gating of the nuclear pore complex (Rout et al., 2000).

Several lines of sequence-based and experimental evidence suggest that it is appropriate to regard NF sidearms as unstructured polyelectrolyte chains. The human NF-H sidearm is rich in charged residues (309 of 607 total amino acids) which are nearly evenly split between anionic and cationic (155 and 154, respectively). The situation is similar for NF-M (238 charged out of 504 total amino acids), although there is considerably less balance between anionic and cationic (145 and 93, respectively). In addition to carrying intrinsic charge, NF-H (and to a lesser extent, NF-M) acquires negative charge through serine and threonine phosphorylation (Lee et al., 1988; Strong et al., 2001). Indeed, measurements with squid giant axon NFs suggest that there may be as many as 100 phosphates per NF sidearm, representing nearly maximal phosphorylation of consensus kinase recognition sites (Leapman et al., 1997). This heavy phosphorylation is critical to modulating the radius of gyration of purified sidearm domains (Chin et al., 1989), reconstituted NF gel properties (Eyer and Leterrier, 1988; Gou et al., 1998), and interfilament spacing in vivo (de-Waegh et al., 1992; Nixon et al., 1994; Yin et al., 1998; Strong et al., 2001). Both the human NF-M and NF-H sidearms are proline-rich (6.2% in NF-M and 13% in NF-H) and low-complexity (Wootton and Federhen, 1996), and are predicted to be devoid of extensive stretches of helix or sheet (Rost and Sander, 1993, 1994). All three of these properties are widely observed in sequences of polypeptides that have been experimentally demonstrated to be unstructured (Uversky et al., 2000; Romero et al., 2001). Finally, a neural network predictor has been developed to identify from databases long, disordered regions of proteins in which the training set consists of sequences from the Protein Databank that are absent in crystal structures. Screening of the entire Swiss-Prot database, which contained nearly 59,000 total sequences when the study was performed, identified the murine NF-H sidearm domain as the sixth-highest scoring sequence (Romero et al., 1998).

In addition to the AFM data discussed earlier, substantial experimental evidence indicates that the NF sidearms are unstructured. No three-dimensional atomic structure for either the NF-H or NF-M sidearm has been reported despite the availability of sequence data and expression systems for over a decade. Circular dichroism measurements show that the bovine NF-M and NF-H sidearm domains contain less than 20% helical content (Chin et al., 1983). Size exclusion chromatography demonstrates that the Stokes radius of the bovine NF-M and NF-H sidearms are 52 and 60 Å, respectively, much larger than expected for sequences of those molecular weights (Georges and Musynski, 1987). Finally, in negative-stain EM, the NF sidearms appear as extended, unfolded structures that reach out 75–100 nm from the NF

core (Geisler and Weber, 1981; Willard and Simon, 1981; Hisanga and Hirokawa, 1988).

Relating structure to interaction potentials in NF distributions

NF organization in the axon is determined by interfilament interactions. We can describe this organization by considering the distribution of NFs in an axonal cross section. The spatial distribution in cross section is quantified by the radial distribution function or two-body correlation function, (RDF, $g(r)$),which is the local density of NFs around a central NF. $g(r)$ is defined as the conditional probability of finding an NF at a distance r given an NF at $r = 0$; the probability is normalized by the average density of NFs in cross-section. The RDF is directly related to the potential of mean force (u_{MF}) for NFs in cross-section through the expression $u_{MF} = -kT \ln g(r)$, where kT is the thermal energy. The potential of mean force is defined as the interaction potential between two NFs averaged over all configurations and orientations of all other NFs in the distribution. In the dilute limit, $u_{MF}(r) = u_{12}(r)$, the pair potential between two isolated NFs. At higher NF densities, two NFs can also interact indirectly through more proximal NFs, producing long-range structure.

Several approaches allow one to relate interaction potentials to the structure of protein or particle distributions, including experimental techniques such as neutron and x-ray scattering or computational methods based on simulation and the application of integral equations (Perelson, 1978, Braun et al., 1984, 1987; Pearson et al., 1983; Pusztai and Toth, 1991; Genz et al., 1994; Toth and Baranyi, 1997). A more recently developed approach relates interparticle correlations to local density fluctuations in the configuration (Hummer et al., 1996, 1998; Garde et al., 2000). Here, one starts with an ensemble of configurations, in our case cross-sectional distributions of NFs in axons. An "observation area" of defined shape and size is randomly placed at a large number of positions in the distribution, the number of particles (n) that fall within each area is counted, and the distribution of occupancy probabilities (occupancy probability distribution, OPD) is calculated. The moments of the resulting probability distribution are related to the physical properties of the system, including density, $g(r)$, and higher-order correlation functions. In general, the nth order moment of the OPD contains information about n-body and lower order correlations. By obtaining experimental OPDs and fitting the data to the predictions of information theory, one may indirectly measure $g(r)$. In practice, this approach tends to be highly robust and relatively tolerant to poor statistics. In addition, because the central measurement involves the counting of particles within a defined area rather than the measurement of interparticle distances, wall effects may be minimized through judicious placement of observation windows.

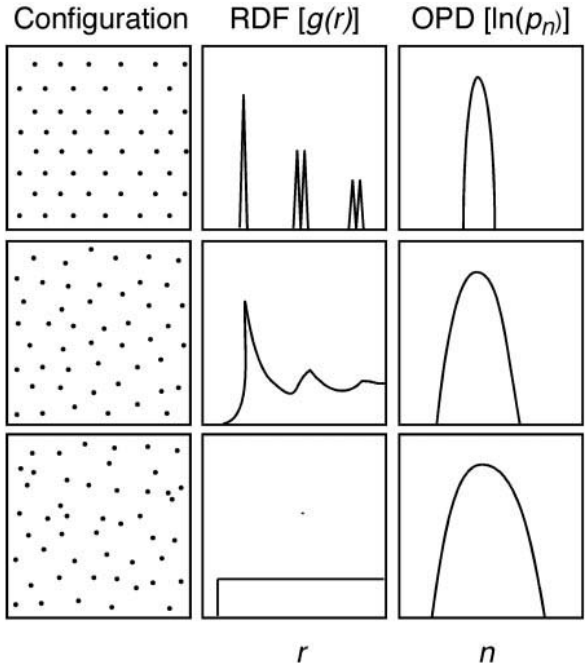

FIGURE 2 Relationship among structure, radial distribution functions, and probability distributions. The top three panels represent a crystalline arrangement, where interfilament spacings occur at precisely defined intervals. The RDF shows sharp spikes, and, for an appropriate and fixed choice of observation area, the OPD is quite narrow. The middle three panels represent a liquid-like NF distribution, in which there is order on relatively short length scales only. Broad maxima are seen in the RDF, and the OPD is broader than for the crystal. The bottom three panels represent an effectively ideal (noninteracting) NF distribution. The NFs are randomly organized, the RDF shows no structure beyond excluded volume, and the OPD is quite broad.

Measurement of the RDF directly through interparticle distances and indirectly through OPDs complement one another (Fig. 2). Direct measurement of the RDF is sensitive to changes in the pair potential but tends to be quite noisy in the absence of large pair statistics. Conversely, the OPD is not as sensitive to the interaction potential but is smooth and fairly easily interpreted even with modest statistics. Both the RDF and OPD are readily measured from particle configurations, and both may be directly compared to the results of simulation in which one imposes a pair potential. Thus, analysis of RDFs and OPDs together can provide structural insights beyond those obtained from either metric alone. We apply this complementary approach to relate experimentally observed distributions of NFs within an axon to physical models of interfilament interactions via pair potentials obtained from polymer brush theory. Specifically, we examine interaction potentials in which the sidearms are modeled as a neutral polymer brush, a polyelectrolyte brush, and a telechelic brush. Monte Carlo (MC) simulation is then used to obtain RDFs and OPDs for each model, which are compared to experiment.

THEORY

Information theory

The OPD (p_n, where $n = 0, \ldots, N$) is analyzed by defining an information entropy $\eta = \Sigma_{n=0}^{N} p_n \ln(p_n/\hat{p}_n)$. Here, $\hat{p}_n$ is a set of known (prior) distributions, which we chose to be unbiased (constant $\hat{p}_n$). The most likely p_n distribution is obtained by maximizing η under constraints that satisfy conditions imposed by the moments of the distribution. Specifically, for the zeroth moment $\langle n^0 \rangle = \Sigma\, p_n = 1$, for the first moment $\langle n^1 \rangle = \Sigma\, n p_n = \pi \Delta A$, where ρ is the number density of NFs in cross section and ΔA is the observation area, and for the second moment $\langle n^2 \rangle = \Sigma\, n^2 p_n = \langle n \rangle + \rho^2 \int_{\Delta A} d\bar{r} \int_{\Delta A} g(|\bar{r} - \bar{r}'|)\, d\bar{r}'$. Including only these moments leads to a Gaussian distribution for p_n, which implies that organization in the system may be described in terms of the cross-sectional density and pair potential of mean force. Higher order correlations involving three or more NFs are not required to describe the structure. The first moment or mean of this Gaussian distribution corresponds to the NF number density in cross-section, and the variance, which is related to the second moment, provides a measure of the magnitude of the interfilament PMF. For a given density, the more tightly distributed the OPD about the mean (i.e., the smaller the local density fluctuations), the stronger the pair correlations between NFs.

Models of NF-NF interactions

The most appropriate geometry for polymer brush interactions between two NFs would be two parallel cylinders; however, to our knowledge, parallel-cylinder potentials have not been developed, reported, or experimentally tested for any of the models described here. We therefore chose sphere–sphere potentials for several reasons. First, unlike plane–plane interaction potentials, sphere–sphere potentials incorporate curvature effects. Second, many spherical potentials have been analytically derived by others, or experimentally verified, or both. Finally, based on the similarity of functional forms for these interactions, the sphere–sphere geometry may be regarded as a reasonable approximation of the cylinder–cylinder geometry (J. Israelachvili, personal communication).

All models used here were developed in the same manner. We start with an analytical expression for the free energy F_P of two brush-covered parallel plates as a function of the separation distance, D. The potential $U_P(D)$ between two such plates is $U_p = F_P - F_{P\infty}$ where $F_{P\infty}$ is the free energy of the plates at infinite separation (equivalent to twice the self-energy of a single plate). We then apply the Derjaguin approximation (Israelachvili, 1992) to convert the plane–plane interaction potential to a sphere–sphere potential, $U_S(r)$, where r is the center-to-center separation distance between the spheres,

$$U_s(r) = \pi \alpha R_c \int_{r-2R_c}^{2L} U_p\, dD. \tag{1}$$

Here, R_c is the radius of the hard NF core, and L is the equilibrium thickness of the sidearm (brush) layer. We also introduce α, a dimensionless constant determined empirically for each interaction potential, to accommodate the use of these expressions, which have been derived based on scaling theories. As a first approximation, we ignore variations along the axial (longitudinal) dimension of the NF. In each case, the NF cross sections were represented by two-dimensional disks, with hard-core area fractions equal to the experimentally obtained cross-sectional area occupied by the NF backbones. All of the potentials are radially symmetric. This approximation is appropriate because in vivo, NFs run in parallel with effective persistence lengths of at least several hundred nanometers. Because, as noted earlier, NF sidearms are spaced ~3–4 nm apart on the backbone, there are tens to hundreds of sidearms per persistence length projecting in a complete range of radial angles from the NF backbone. The length scale on which there are appreciable radial variations in effective sidearm density are therefore small compared to typical NF–NF separation distances; thus, radial variations in the interaction potential are neglected.

Alexander–DeGennes potential

In the Alexander–DeGennes framework, the brush is assumed to have a uniform (step) monomer density profile. The equilibrium brush thickness is determined by the relative strength of two competing forces: the osmotic pressure of the chain monomers that tends to swell and expand the brush, and chain elasticity, which acts to oppose this swelling. In the expression for the interaction potential between two brush-coated surfaces, L is a composite parameter that incorporates information about monomer dimensions and chain length. We based our potential on the expression developed by Likos et al. (2000). This potential has been found to account for structure factors for polypeptide-coated spheres obtained from small-angle neutron scattering. Here y is the dimensionless distance $(r - 2R_c)/2L$, where L is the equilibrium brush thickness,

$$\begin{aligned}
\beta U_s(y) &= \infty \quad \text{for} \quad y \le 0 \\
&= \alpha_{AD} \frac{16 \pi R_c L^2}{35 s^3} \left[28(y^{-1/4} - 1) + \frac{20}{11}(1 - y^{11/4}) \right. \\
&\qquad \left. + 12(y - 1) \right] \quad \text{for} \quad 0 < y \le 1 \\
&= 0 \quad \text{for} \quad y > 1.
\end{aligned} \tag{2}$$

Here, $\beta = 1/kT$, and s is the distance between chains on the grafting surface.

Self-consistent field potential

In the self-consistent field (SCF) description of a polymer brush, the discrete monomers are represented through a field theoretical approach. Perhaps the most widely implemented potential of this type is that of Milner et al. (1988). Starting with this expression, we developed an SCF-based interaction potential for NFs. This plane–plane potential has been adapted to the sphere–sphere geometry and used to model rheologic data for entropically stabilized particles (Mewis et al., 1989). In our simulations, we used

$$\begin{aligned}\beta U_s(y) &= \infty \quad \text{for} \quad y \le 0 \\ &= \alpha_{SCF}\left(\frac{L}{a}\right)^3 R_C N^{-1/2} s^{-2}\left(\frac{\pi^3}{12}\right) \\ &\quad \times \left(-\ln(y) + \frac{1}{3}(1-y^3) - \frac{1}{30}(1-y^6)\right. \\ &\quad \left. - \frac{9}{5}(1-y)\right) \quad \text{for} \quad 0 < y \le 1 \\ &= 0 \quad \text{for} \quad y > 1. \end{aligned} \tag{3}$$

Here, N is the number of monomers per chain, a is the monomer length, and L is determined by the expression,

$$L = \left(\frac{12}{\pi^2}\right)^{1/3} Na\left(\frac{v}{as^2}\right)^{1/3}, \tag{4}$$

where v is the monomer volume taken to be a^3 as a first approximation, and α_{SCF} is as before.

Polyelectrolyte brush potential

To incorporate the effects of chain charge into our model, we implemented a pair potential function that follows the scaling analysis of Pincus (1991). Here, brush structure is governed by the competing influences of monomer–monomer electrostatic repulsion and osmotic pressure, which tend to swell the brush, and chain elasticity, which opposes brush expansion. The model is for two plates grafted with a uniform layer of polyelectrolytes each composed of N monomers of length a, a fraction f of which are charged, in the presence of salt concentration c_s. The disjoining (osmotic) pressure (Π) for such a system is given by

$$\beta\Pi \approx 2N^2/(s^4 c_s D^2). \tag{5}$$

To obtain the free energy, we integrate with respect to D,

$$\beta F_p = 2N^2/(s^4 c_s D). \tag{6}$$

Invoking the Derjaguin approximation as above, we find,

$$\beta U_s(y) = \alpha_{PE}[2\pi R_c N^2/(s^4 c_s)]\ln(y), \tag{7}$$

where, again, the dimensionless distance y is used, and α_{PE} is the scaling factor.

Telechelic brush potential

Telechelic brushes are composed of chemically bifunctional molecules. One end binds the grafting surface, and the other is free to bind other chains, either within the brush or in an apposing brush. Experimental studies with the surface forces apparatus show that telechelic brushes retain the long-range repulsion characteristic of polymer brushes but enter an attractive regime when the brushes are brought into contact. Thus, telechelic brushes serve as an appropriate physical model for cross-bridging interactions. For the repulsive component of the interaction potential, we retained the Pincus expression used earlier. We begin with the expression developed by Zilman and Safran (2001) for the interaction potential between two plates coated with telechelic (end-associating) brushes,

$$\beta F_P = \beta F_{rep} - \beta\epsilon N_s, \tag{8}$$

where F_{rep} is a repulsive flat-plate polymer brush interaction potential (taken here to be the expression for polyelectrolyte brushes developed above), and ϵ is the energy of association per unit area. N_s is the number of chain ends in contact per unit area, given by $N_s = 4N^{-1/2}\sigma^{5/6}(1-u^2)u^{1/2}$, where, $u = D/(2L)$ and $\sigma = a^2/s^2$. These expressions assume that intrafilament cross bridging is far less prevalent than interfilament cross bridging and that the chains in adjacent brushes do not interdigitate. Applying the Derjaguin approximation, we find,

$$\begin{aligned}\beta U(y) &= \beta U_{PE}(y) \\ &\quad - \alpha_{tel}\epsilon 2\pi R_c L\left[\tfrac{2}{3}(1-y^{3/2}) - \tfrac{2}{7}(1-y^{7/2})\right], \end{aligned} \tag{9}$$

where $U_{PE}(y)$ is the sphere–sphere interaction potential for interacting polyelectrolyte brushes.

Choices of polymer parameters

Polymer parameters were chosen to reflect the known physical dimensions of the murine NF-H sidearm. We took $N = 679$, the number of amino acids in the tail domain of NF-H. We also set $R_c = 5$ nm and $s = 3$ nm based on estimates from EM of purified single NFs (Geisler and Weber, 1981).

METHODS

Processing electron micrographs

Electron micrographs of sciatic nerve cross-sections from 9-month-old mice were obtained as described previously (Yin et al., 1998). Each EM

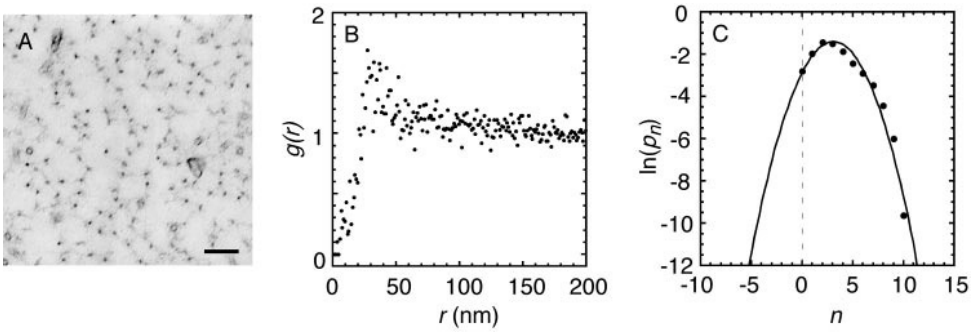

FIGURE 3 Statistical characterization of NF distributions from mouse sciatic nerve. (*A*) EM of mouse sciatic nerve cross section at 9 months. The NFs are the dark, pointlike structures. (Bar is 100 nm). Note that, although other cellular elements such as microtubules and organelles are shown to accurately represent the cross section, regions depleted in these elements were chosen for analysis. (*B*) RDF. (*C*) OPD for observation circle of radius 60 nm. The points represent experimentally obtained values, and the line corresponds to the predicted Gaussian fits of information theory. Each plot is a number-weighted average of EMs from six axons containing 200-1000 NFs each.

was scanned into an image file and then digitized. A rectangular area of 1–5 μm in either dimension was identified, in each case, completely within the axoplasm and relatively free of microtubules and other organelles. The position of each NF within this defined area was then identified by hand and recorded, resulting in a set of pair coordinates. These coordinates were then used to calculate OPDs and RDFs as described below. The RDF and OPD from six micrographs containing 200-1000 NFs each were weighted according to the number of NFs in each micrograph and averaged.

Monte Carlo simulation

NFs were represented as two-dimensional disks in canonical ensemble Metropolis MC simulations in which particles interacted through the radially-symmetric pair potentials described above. The disks were initially placed in a square lattice at a number density corresponding to axonal NFs. One MC move consisted of a single randomly-chosen particle displaced in both x and y within a fixed range. The total energy of the configuration was calculated assuming additivity of all pair energies. Periodic boundary conditions were enforced. A MC cycle consisted of a number of MC moves equal to the number of disks. After equilibration, as judged by constant energy and radial distribution function, distributions were accumulated every 10–15 cycles and averaged at the completion of the simulation to calculate RDFs and OPDs.

Calculation of radial distribution functions

Disk–disk distances were calculated in a pairwise manner. These distances were then binned and normalized by a factor proportional to the number of particles and the separation distance to yield $g(r)$. Calculation of $g(r)$ in a system of finite size introduces the possibility of artifacts due to the presence of walls. Several solutions have been proposed and implemented to address this, including the use of periodic boundaries (Allen and Tildesley, 1987) and normalizing against a randomly-distributed distribution (Pearson et al., 1983). After trying both of these methods, we found that periodic boundaries yielded the most robust results within reasonable computation times. Results were reproducible over a reasonable range of bin sizes, with the expected increase in noise with decreasing bin width.

Calculation of occupancy probability distributions

A circular observation area of fixed radius (60 nm unless stated) was placed at a random location within each distribution, and the particle occupancy number for each observation was recorded. This process was repeated many times (typically 10–20 times the number of particles), producing a histogram of occupancy numbers. This histogram was normalized by the number of observations to yield the OPD. In all cases, Gaussian fits were performed as parabolic fits to $\ln(p_n)$.

RESULTS

When the sciatic nerve of a 9-month-old mouse is sectioned and its constituent axons are visualized by EM, an ordered distribution of point-like structures is revealed (Fig. 3 *A*). Each of these structures is the cross section of an individual NF. To quantify NF organization, we calculated both RDFs (Fig. 3 *B*) and OPDs (Fig. 3 *C*). The RDF appears noisy because of the necessity for a small bin size (1 nm) in combination with the finite experimental data. The values of $g(r)$ at distances less than 10 nm approach zero, which is consistent with measurements of isolated NFs by EM that demonstrate an excluded volume diameter of 8–12 nm (Geisler and Weber, 1981). The deviation of these values from zero reflects both the noise in these $g(r)$ calculations and measurement uncertainties at small separation distances. Two key features of the RDF are the position of the first peak (r_{max}) and its magnitude (g_{max}). The most prominent feature of the RDF is a gradually developing maximum with $g_{max} > 1$ at r_{max} at 30–45 nm, consistent with previously measured distributions of nearest-neighbor interfilament spacings for mice of this age (Yin et al., 1998). The OPD, in turn, is well described by a Gaussian distribution with a mean of 2.6 and a standard deviation of 1.7. Within a robust range, the Gaussian description holds independent of the choice of observation window radius (varied between ~50 and 100 nm, not shown). Taken together, these experimental findings show order in the system that can be described using only the NF cross-sectional density and the NF–NF pair potential of mean force. This motivates our representation of the system in Monte Carlo simulations by a radially symmetric NF–NF pair potential that characterizes NF organization.

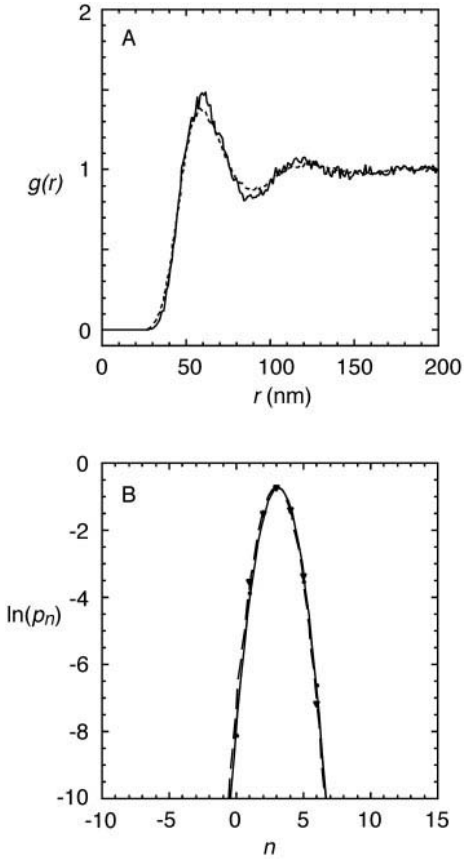

FIGURE 4 Representation of NF sidearms as neutral polymer chains. The sidearms were modeled to interact according to the Alexander–DeGennes potential (*solid lines*) and self-consistent field potential (*dashed lines*) for neutral polymer brushes. (*A*) RDFs. (*B*) OPDs. In (*B*), the points represent the results from simulation, and the lines represent Gaussian fits.

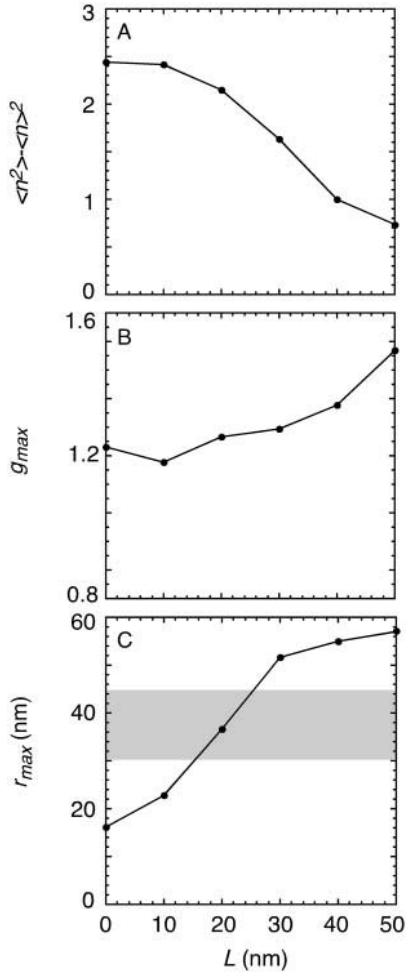

FIGURE 5 Effect of equilibrium brush thickness on structure in NF distributions. The equilibrium brush thickness (L) was systematically varied, and several descriptors of $g(r)$ and p_n were examined. (*A*) $\langle n^2\rangle - \langle n\rangle^2$. For a Gaussian curve, this corresponds to the variance, which decreases with stronger interfilament correlations. (*B*) The magnitude of the first maximum in $g(r)$ (g_{max}). This is a metric for structure at distances corresponding to nearest-neighbor spacing. (*C*) The interfilament distance (r_{max}) at which the maximum value of $g(r)$ is reached. The shaded area corresponds to the range of interfilament distances covered by the first peak in the experimental RDF (shown in Fig. 1), and, as such, gives a range over which NF–NF spacing is expected to be controlled by the model.

We next implemented two neutral polymer brush models (Alexander–DeGennes and self-consistent field descriptions) in Monte Carlo simulations and calculated the resulting RDF (Fig. 4 *A*) and OPD (Fig. 4 *B*). Both models produce RDFs with gradually developing first peaks at 50–60 nm. It is interesting to note that the scaling parameter (α) needed to superimpose the data with the SCF potential (3×10^{-7}) was much smaller than for Alexander–DeGennes potential (0.05). These parameters are expected to differ because the Alexander–DeGennes expression is itself obtained from scaling arguments. A physical interpretation of this difference is discussed below. For both potentials, r_{max} is 10–15 nm greater than the experimentally obtained value. The value of g_{max} is in reasonable agreement with experiment. However, given the marked scatter in the experimental data, anything more than a qualitative comparison of these features of the RDFs is not possible. The experimental OPD, by contrast, is much more amenable to comparison with simulation. Both models produce Gaussian OPDs with mean occupancies of 2.7, as expected by the fixed NF density. The variances of the two OPDs from simulation are identical to one another but are somewhat smaller than the experimental OPD.

To examine the effects of brush properties on the NF distribution, we conducted additional simulations in which only the equilibrium brush thickness (L) was varied in the Alexander–DeGennes expression. Changes in the radial distribution functions are tracked by examining the primary peak position and magnitude in $g(r)$ and the variance of the OPD. As the brush thickness is increased, the variance of the OPD falls, a signature of stronger pair correlations and smaller local density fluctuations (Fig. 5 *A*). Consistent with this result are the changes in the RDFs. As the brush thickness is increased, the distribution develops structure,

and this structure shifts to greater distances (Fig. 5, *B* and *C*). At the lowest values of L, as the effective NF cross-sectional density decreases, structure disappears with g_{max} approaching the hard-sphere limit. Physiologically, r_{max} corresponds to favored nearest-neighbor interfilament spacings. The values obtained from simulation are in agreement with the range of these values observed in our system (Fig. 1), and, more generally, for a variety of axonal systems (deWaegh et al., 1992; Lee and Cleveland, 1996). Thus, changes in brush thickness can affect structure in cross-sectional NF distributions by increasing the range of interfilament interactions and increasing effective NF density.

Because the Alexander–DeGennes potential collapses monomer properties (size, charge, etc.) into the parameter L, one cannot directly probe the effects of independently changing these microscopic parameters on brush structure. This is important to the extent that the NF sidearms acquire a substantial net negative charge from extensive serine phosphorylation of NF-H, and much evidence from studies in vitro and in vivo implicates the degree of NF-H phosphorylation as an important regulator of interfilament spacing. To explore these effects, we conducted simulations in which the NF sidearms were represented as polyelectrolytes. When all serines in the murine NF-H tail sequence are phosphorylated, it bears a fractional charge of 0.067. As the fractional charge is increased to this level, corresponding to successive phosphorylation, the RDF gains structure (Fig. 6 *A*). The basis for this change is the increase in equilibrium brush thickness, which rises linearly with fractional charge according to the Pincus formalism. This is illustrated by the narrower OPDs with increasing fractional charge (Figs. 6 *B* and 7 *A*), which mirrors the observed dependence when the brush thickness was directly manipulated through the parameter L in the Alexander–DeGennes potential. As the range of interfilament repulsion rises, pair correlations become stronger and local fluctuations in density are reduced. Likewise, the parameters describing the RDF change systematically. As the fractional charge is increased, we observe a graded increase in structure (Fig. 7 *B*) and a shift to greater favored NF–NF separation distances (Fig. 7 *C*). Moreover, changes in fractional charge produce changes in NF–NF spacing that correspond to the range of the first maximum in the experimental RDF (Fig. 1). According to all three metrics of NF organization, structure changes in a gradual manner over a physiologic range of phosphorylation.

The preceding results support the notion that a purely repulsive force imparts structure to NF distributions observed in axons and that a phosphorylation/dephosphorylation mechanism can control the range of this repulsion and thereby the organization of the distribution. A potential based on this physical model yields NF distributions that are consistent with experimentally measured values. We next examined the effect of superimposing attractive cross-bridging interactions onto a repulsive potential through a telechelic brush model (Fig. 8). Modeling cross bridging as a telechelic brush-like interaction produces an NF–NF attractive component in the potential. The choice of this model was motivated in part by a previous report in which we represented these interactions in terms of a square-well attractive potential. There, we found that the discontinuity in the square-well potential results in prominent spikes in the RDF that are inconsistent with the experimental data (S. Kumar, X. Yin, B. D. Trapp, M. E. Paulaitis, and J. H. Hoh, submitted for publication). In molecular terms, superimposing an increasingly attractive component onto the repulsive potential is equivalent to either increasing the energy of individual cross bridges or increasing the number of cross bridges at a fixed energy. As the attractive component is increased incrementally to $\sim 30kT$, neither the RDF nor the OPD change appreciably, in contrast to the observed physiological range of change. The width of the OPD essentially remains constant. There is a small decrease in g_{max} and an increase in r_{max}, reflecting the greater sensitivity of the RDF to changes in potential.

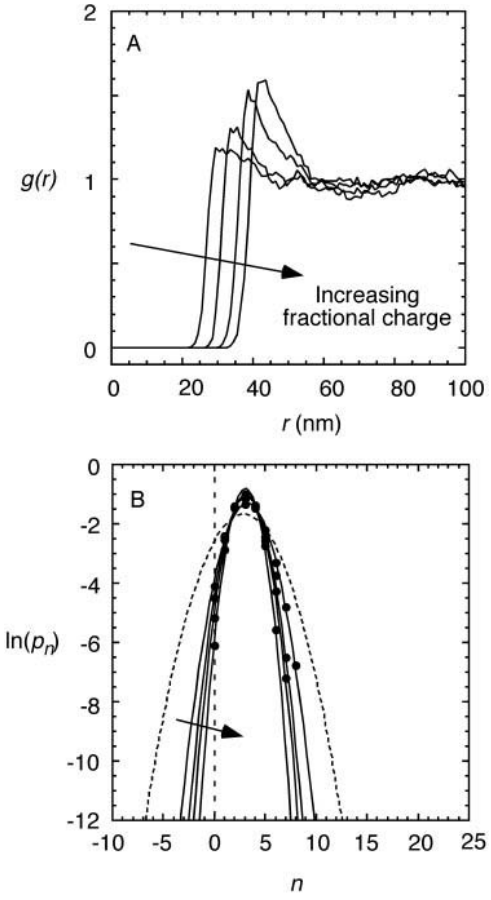

FIGURE 6 Effect of sidearm charge on structure in NF distributions. The fractional charge was increased to 0.067, corresponding to successive phosphorylation to the fully phosphorylated NF sidearm. (*A*) RDFs. (*B*) OPDs. The Gaussian for the experimental data (*broken line*) is reproduced here as a guide. In each case, the arrow indicates the direction of increasing fractional charge.

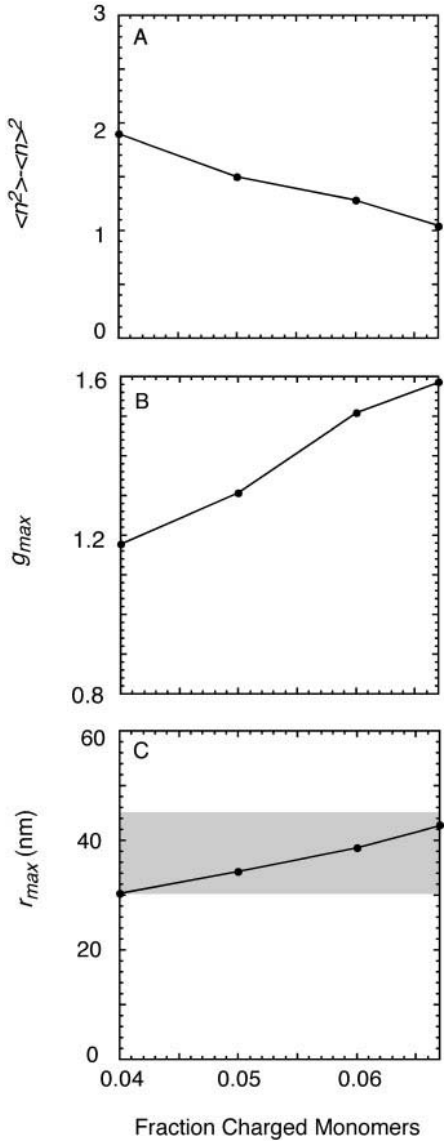

FIGURE 7 Variation of RDF and OPD parameters with sidearm phosphorylation. (*A*) $\langle n^2\rangle - \langle n\rangle$, (*B*) g_{max}, and (*C*) r_{max}. The maximum charge here (0.067) approximately corresponds to complete phosphorylation of the NF-H sidearm. As the charge is increased up to this value, NF–NF pair correlations rise as a result of stronger interfilament repulsion, and the position of the favored NF–NF spacing increases. The shaded area in (*C*) is as described for Fig. 5.

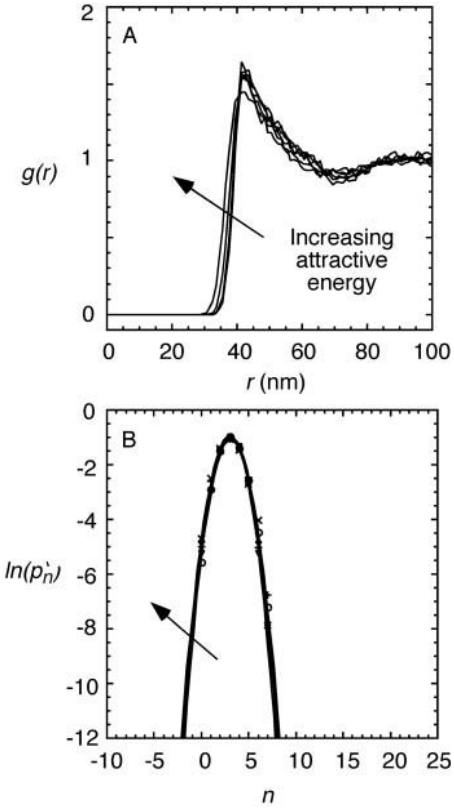

FIGURE 8 Effect of NF–NF attractive interactions on structure in NF distributions: moderate cross bridging. The repulsive component of the interaction potential was fixed at the values corresponding to a fractional charge of 0.067, and the attractive energy was increased up to a total of ~30*kT* per NF pair through a formalism in which the sidearms were treated as telechelic (associative) polymers. (*A*) RDFs. For modest increases in NF attractive forces, few changes are observed in the first peak of $g(r)$. (*B*) OPDs. In each case, the arrow points in the direction of increasing attraction. Neither the RDF nor the OPD changes appreciably in this regime of attractive energies.

As the attractive component is increased beyond 70–80*kT* per NF pair, an abrupt transition is observed in the RDF and OPD. g_{max} is an order of magnitude greater than that observed for cross-bridging interactions up to 30*kT*, and the radius corresponding to the effective excluded volume is twice the NF backbone radius ($r = 10$ nm) (Fig. 9 *A*). Visual inspection of a configuration sampled during the simulation reveals that this is due to extensive NF aggregation (*inset*). The OPD deviates dramatically from a Gaussian distribution, with a maximum occupancy probability at $n = 0$, which reflects the dominance of voids left as a result of aggregation. Further, the large deviation from Gaussian behavior indicates that pair correlations in the context of the information theory framework cannot describe the organization. At these high attractive energies, the shape and magnitude of the RDF and OPD differ substantially from the experimental results, suggesting that attractive energies in this regime yield unrealistic descriptions of axonal NF organization. This justifies setting 70*kT* as a maximum cutoff below which the effect of NF cross bridging as a structural determinant may be examined.

We therefore varied the attractive component between 0 and 70*kT* and examined the effect on the parameters of the RDF and OPD (Fig. 10). There is very little change in either the variance of the OPD over this range of attractive energies (Fig. 10 *A*) or the position of the first peak in the RDF (Fig. 10 *C*). In particular, coverage of the range of r_{max} observed in the experimental RDF is poor. The primary maximum of the RDF does decrease modestly as the attractive energy is increased (Fig. 10 *B*). However, the observed

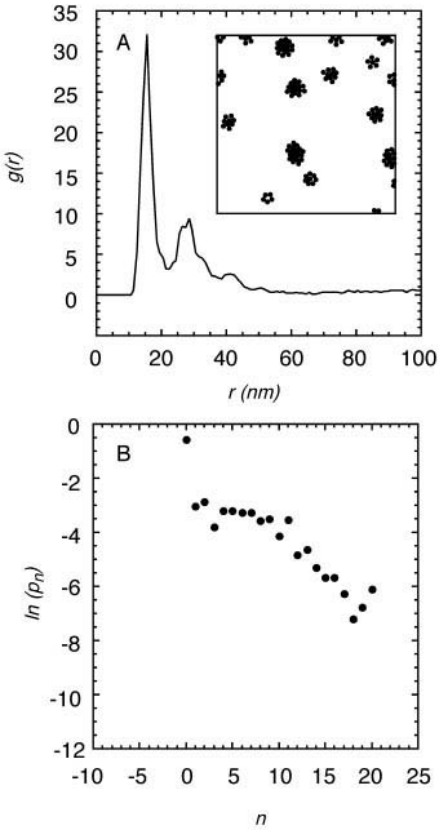

FIGURE 9 Effect of NF–NF attractive interactions on structure in NF distributions: strong cross bridging. When the NF–NF attractive energy is increased beyond $70-80kT$, an abrupt phase transition occurs, leading to characteristic changes in the RDF and OPD. (*A*) RDF for attractive component of $150kT$. Inspection of a sample configuration (*inset*) reveals NF–NF aggregation and phase separation. (*B*) OPD for the same pair potential. The pronounced maximum at $n = 0$ and the non-Gaussian shape reflect the large void spaces induced by NF–NF aggregation.

direction of change is toward decreasing NF–NF organization with increasing cross bridging, which is opposite from that predicted by NF cross-bridging models (Gotow et al., 1994). We find that increasing attractive cross-bridging interactions in a physiologically realistic regime does not significantly influence NF organization. Where effects are seen, they regulate NF organization in a manner opposite that predicted by the underlying physical model. That is, cross bridging diminishes the organizing influence of repulsive interactions. Therefore, these results do not support the cross-bridging hypothesis.

DISCUSSION

Several key findings emerge from the analysis of NF distributions. In particular, the RDFs show first peak positions consistent with measured mean nearest-neighbor interfilament distances. The experimental OPDs are well described by a Gaussian distribution, motivating the representation of the NF distributions in terms of a density and pair potential

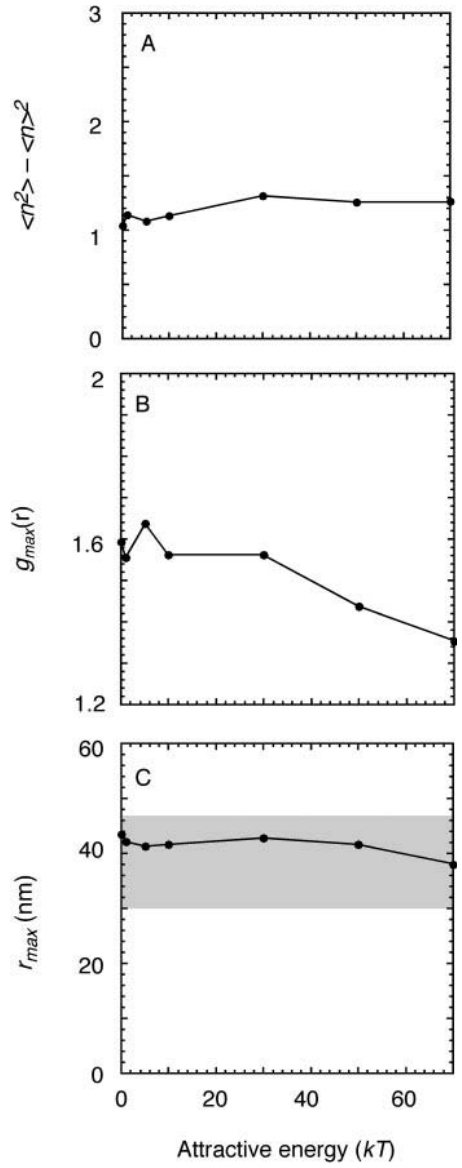

FIGURE 10 Variation of RDF and OPD parameters with sidearm cross bridging. Changes in NF distribution structure parameters with increases in NF–NF attraction for levels of cross bridging that are not sufficiently strong to induce aggregation. (*A*) $\langle n^2\rangle - \langle n\rangle^2$. (*B*) g_{max}. (*C*) r_{max}. There is little change in any of the parameters over this range of attractive energies. At the highest energies, the attraction counteracts the repulsive forces and reduces NF–NF correlations. The shaded area in (*C*) is as described for Figs. 5 and 7.

of mean force. The use of interaction potentials, in which the sidearms are represented as neutral polymer chains, provides RDFs and OPDs that reproduce the general features in the experimental data. All of the physical parameters in these models may be reliably estimated from existing structural data. With respect to the scaling constant α, we find that a much smaller prefactor is needed for the SCF potential to describe the data than for the Alexander–De-Gennes potential. Given the scaling arguments used to de-

termine these potentials, the disparity in prefactors is not surprising; the differences in which each model treats the monomer density profile may also play a role. Indeed, direct comparison of the compressive forces predicted by each model shows that the SCF force is both greater and more long range than the Alexander–DeGennes force (Milner et al., 1988). Simulations in which the brush thickness was systematically varied reveal that increases in brush thickness produce increases in the structure of the NF distribution. This immediately suggests that changes in sidearm expansion may serve to regulate interfilament spacing and NF organization. This notion has been invoked in the context of cross-bridging models, where the sidearms have been hypothesized to "extend" or "unfold" under increasing phosphorylation, leading to increased cross-bridging distances (Jaffe et al., 2001). However, the data presented here show that sidearm extension itself, not changes in cross-bridging dimensions, determines axonal NF structure.

The simulation results implicate phosphorylation as a mechanism for controlling sidearm expansion. As the fractional charge along the sidearm is increased through the physiologically observed range, we observe dramatic changes in NF organization both by RDFs and by OPDs. This is consistent with a mechanism in which increased sidearm phosphorylation produces an expanded brush through local electrostatic and osmotic interactions. As discussed earlier, much evidence supports sidearm phosphorylation as an important regulator of interfilament spacing. Our results support a mechanism by which phosphorylation serves as a biochemical regulator (i.e., a graded switch) that controls interfilament spacing by expanding or collapsing the sidearm brush. Cross bridging may occur between NFs, but there is no evidence here that they contribute to structure in the context of a preexisting repulsive potential. This finding is consistent with previous efforts to model cytoskeletal interactions, which suggest that soft electrostatic repulsion between dilute cylindrical particles can generate considerable long-range order (Kramer and Herzfeld, 2000), and cross-linking proteins primarily serve to stabilize the relative orientations of individual filaments rather than drive their organization (Herzfeld, 1996).

Cross-linking has been invoked as an important regulatory force for actin and intermediate filament networks (Coulombe et al., 2000, Mullins et al., 1998). An emerging theme for many of these networks is that structural and mechanical properties are controlled by many relatively low-affinity cross-links, allowing rapid changes in cell shape and viscoelasticity. Therefore, one might expect that, if cross bridging were a critical regulator of axonal NF structure, one would observe significant changes in this structure over a range of small binding energies. Instead, our simulations with telechelic brush potential functions predict only modest changes in structure for attractive energies up to $\sim 70kT$. When the cross-bridging energy is increased beyond this threshold, the simulations demonstrate extensive NF aggregation.

Although it is unlikely that NFs in healthy axons ever aggregate to the extent observed here, the simulations in this regime suggest a connection between dominant attractive forces in general and mechanisms of NF pathology. Several studies show that NF aggregation in neurodegeneration is accompanied by increases in intracellular calcium concentrations (Cassarino et al., 1999), whereas others have shown that multivalent cations can induce NF aggregation in vitro (Leterrier et al., 1992). Moreover, normally repulsive polyelectrolyte brushes can be induced to attract in the presence of divalent cations (Tamashiro et al., 2001). One may therefore postulate a pathological process in which the normally repulsive NF–NF interaction is made attractive through a large, local increase in multivalent cation concentration, leading to aggregation.

In our depiction of cross-bridging interactions, we neglect cross bridging between sidearms on the same filament (i.e., intrafilament cross bridging) as a positive structural determinant. This is justified for several reasons. First, the structures reported in EM studies are largely inter- rather than intrafilament cross bridges. Second, in cases where intrafilament cross-bridging models have been invoked, such cross bridges are proposed to weaken rather than strengthen interfilament interactions by making the sidearms less available to adjacent NFs (Gou et al., 1998). Although our data do not support interfilament cross-bridging as a significant contributor to NF structure, net increases in intrafilament interactions, i.e., reductions in NF sidearm brush thickness, weaken interfilament interactions and diminish axonal NF structure.

Both the RDF and the OPD yield important structural information about the organization of NF cross-sections, although the RDFs show considerably more experimental noise than the OPDs. Several factors account for this. First, the RDF is more sensitive than the OPD to the noise produced by the relatively limited experimental sample size. Second, the OPD incorporates pair correlations through an integrated form of the RDF, via the second moment of the OPD. This integration tends to average out the noise in the RDF, leading to smooth probability distributions. An important tradeoff, however, is that the OPD tends to be less sensitive to changes in interaction potentials than does the RDF. This is evidenced by the simulations with telechelic brush models in the regime of moderate attractive energy, in which the RDF shows modest changes with increasing attraction but in which changes in the OPD are essentially negligible.

Finally, it is interesting to note that all of the repulsive potentials examined here somewhat overpredict structure, particularly at small separation distances. At least three factors contribute to this. First, at small NF–NF separations, these separations begin to approach experimental uncertainties in measuring relative NF positions by EM. Second, the

RDF is calculated by collecting a histogram of NF–NF separation distances and normalizing by a factor that is itself proportional to separation distance. Thus, these two factors tend to magnify errors in measurements of small separation distances. Third, the infinitely steep repulsion included in these interaction potentials produces artificially stringent exclusion volumes at small separations. This phenomenon has been observed in neutron scattering studies of flexible dendrimers, in which hard-wall potentials were found to substantially overpredict the first peak in the structure factor. In those studies, the Gaussian core model (GCM), a considerably softer interaction potential, was found to improve the description of the data (Likos et al., 2001). To our knowledge, GCM potentials, which explicitly incorporate all of the molecular details relevant to NFs (e.g., chain charge, grafting density), have not yet been developed or implemented for polymer brush interactions. It would be useful to fashion more physically detailed GCM expressions and to check for better agreement with experiment.

This work was supported by grants from the National Institutes of Health (Medical Scientist Training Program fellowship to S.K.; NS38186 to B.D.T.), the U.S. Army (DAMD 17-99-1-9488 to J.H.H.), and the National Science Foundation (CTS-0078491 to M.E.P.).

REFERENCES

Allen, M. P., and D. J. Tildseley. 1987. Computer Simulation of Liquids. Oxford Science Publications, Oxford, U.K.

Braun, J., J. R. Abney, and J. C. Owicki. 1984. How a gap junction maintains its structure. *Nature.* 310:316–318.

Braun, J., J. R. Abney, and J. C. Owicki. 1987. Lateral interactions among membrane-proteins—valid estimates based on freeze–fracture electron-microscopy. *Biophys. J.* 52:427–439.

Brown, H. G., and J. H. Hoh. 1997. Entropic exclusion by neurofilament sidearms: a mechanism for maintaining interfilament spacing. *Biochemistry.* 36:15035–15040.

Cassarino, D. S., and J. P. Bennett. 1999. An evaluation of the role of mitochondria in neurodegenerative diseases: mitochondrial mutations and oxidative pathology, protective nuclear responses, and cell death in neurodegeneration. *Brain Res. Rev.* 29:1–25.

Chen, J. G., T. Nakata, Z. Z. Zhang, and N. Hirokawa. 2000. The C-terminal tail domain of neurofilament protein-H (NF-H) forms the crossbridges and regulates neurofilament bundle formation. *J. Cell Sci.* 113:3861–3869.

Chin, T. K., P. A. M. Eagles, and A. Maggs. 1983. The proteolytic digestion of ox neurofilaments with trypsin and alpha-chymotrypsin. *Biochem. J.* 215:239–252.

Chin, T. K., S. E. Harding, and P. A. M. Eagles. 1989. Characterization of 2 proteolytically derived soluble polypeptides from the neurofilament triplet components NFM and NFH. *Biochem. J.* 264:53–60.

Coulombe, P. A., O. Bousquet, L. Ma, S. Yamada, and D. Wirtz. 2000. The 'ins' and 'outs' of intermediate filament organization. *Trends Cell. Biol.* 10:420–428.

de Waegh, S. M., V. M. Y. Lee, and S. T. Brady. 1992. Local modulation of neurofilament phosphorylation, axonal caliber, and slow axonal transport by myelinating schwann cells. *Cell.* 68:451–463.

Eyer, J., and J. F. Leterrier. 1988. Influence of the phosphorylation state of neurofilament proteins on the interactions between purified filaments in vitro. *Biochem. J.* 252:655–660.

Garde, S., R. Khare, and G. Hummer. 2000. Microscopic density fluctuations and solvation in polymeric fluids. *J. Chem. Phys.* 112:1574–1578.

Geisler, N., and K. Weber. 1981. Self-assembly in vitro of the 68,000 molecular-weight component of the mammalian neurofilament triplet proteins into intermediate-sized filaments. *J. Mol. Biol.* 151:565–571.

Genz, U., B. Daguanno, J. Mewis, and R. Klein. 1994. Structure of sterically stabilized colloids. *Langmuir.* 10:2206–2212.

Georges, E., and W. E. Mushynski. 1987. Chemical modification of charged amino-acid moieties alters the electrophoretic mobilities of neurofilament subunits on SDS polyacrylamide gels. *Eur. J. Biochem.* 165:281–287.

Gotow, T., T. Tanaka, Y. Nakamura, and M. Takeda. 1994. Dephosphorylation of the largest neurofilament subunit protein influences the structure of crossbridges in reassembled neurofilaments. *J. Cell Sci.* 107: 1949–1957.

Gou, J. P., T. Gotow, P. A. Janmey, and J. F. Leterrier. 1998. Regulation of neurofilament interactions in vitro by natural and synthetic polypeptides sharing lys-ser-pro sequences with the heavy neurofilament subunit NF-h: neurofilament crossbridging by antiparallel sidearm overlapping. *Med. Biol. Eng. Comput.* 36:371–387.

Herzfeld, J. 1996. Entropically-driven order in crowded solutions: from liquid crystals to cell biology. *Acc. Chem. Res.* 29:31–37.

Hisanaga, S., and N. Hirokawa. 1988. Structure of the peripheral domains of neurofilaments revealed by low-angle rotary shadowing. *J. Mol. Biol.* 202:297–305.

Hoh, J. H. 1998. Functional protein domains from the thermally driven motion of polypeptide chains: a proposal. *Proteins Struct. Funct. Genet.* 32:223–228.

Hsieh, S. T., T. O. Crawford, and J. W. Griffin. 1994. Neurofilament distribution and organization in the myelinated axons of the peripheral nervous system. *Brain Res.* 642:316–326.

Hummer, G., S. Garde, A. E. Garcia, M. E. Paulaitis, and L. R. Pratt. 1998. Hydrophobic effects on a molecular scale. *J. Phys. Chem. B.* 102: 10469–10482.

Hummer, G., S. Garde, A. E. Garcia, A. Pohorille, and L. R. Pratt. 1996. An information theory model of hydrophobic interactions. *Proc. Natl. Acad. Sci. U.S.A.* 93:8951–8955.

Israelachvili, J. N. 1992. Intermolecular and Surface Forces. Academic Press, New York.

Jaffe, H., P. Sharma, P. Grant, and H. C. Pant. 2001. Characterization of the phosphorylation sites of the squid (*Loligo pealei*) high-molecular-weight neurofilament protein from giant axon axoplasm. *J. Neurochem.* 76: 1022–1031.

Julien, J. P. 1999. Neurofilament functions in health and disease. *Curr. Opin. Neurobiol.* 9:554–560.

Kramer, E. M., and J. Herzfeld. 2000. Avoidance model for soft particles. II. Positional ordering of charged rods. *Phys. Rev. E.* 61:6872–6878.

Leapman, R. D., P. E. Gallant, T. S. Reese, and S. B. Andrews. 1997. Phosphorylation and subunit organization of axonal neurofilaments determined by scanning transmission electron microscopy. *Proc. Natl. Acad. Sci. U.S.A.* 94:7820–7824.

Lee, M. K., and D. W. Cleveland. 1996. Neuronal intermediate filaments. *Annu. Rev. Neurosci.* 19:187–217.

Lee, V. M. Y., L. Otvos, M. J. Carden, M. Hollosi, B. Dietzschold, and R. A. Lazzarini. 1988. Identification of the major multiphosphorylation site in mammalian neurofilaments. *Proc. Natl. Acad. Sci. U.S.A.* 85: 1998–2002.

Lees, J. F., P. S. Shneidman, S. F. Skuntz, M. J. Carden, and R. A. Lazzarini. 1988. The structure and organization of the human heavy neurofilament subunit (NF-H) and the gene encoding it. *EMBO J.* 7:1947–1955.

Leterrier, J. F., and J. Eyer. 1987. Properties of highly viscous gels formed by neurofilaments in vitro—a possible consequence of a specific interfilament cross-bridging. *Biochem. J.* 245:93–101.

Leterrier, J. F., D. Langui, A. Probst, and J. Ulrich. 1992. A molecular mechanism for the induction of neurofilament bundling by aluminum ions. *J. Neurochem.* 58:2060–2070.

Leung, C. L., D. M. Sun, and R. K. H. Liem. 1999. The intermediate filament protein peripherin is the specific interaction partner of mouse BPAG1-n (dystonin) in neurons. *J. Cell Biol.* 144:435–446.

Likos, C. N., M. Schmidt, H. Lowen, M. Ballauff, D. Potschke, and P. Lindner. 2001. Soft interaction between dissolved flexible dendrimers: theory and experiment. *Macromolecules.* 34:2914–2920.

Likos, C. N., K. A. Vaynberg, H. Lowen, and N. J. Wagner. 2000. Colloidal stabilization by adsorbed gelatin. *Langmuir.* 16:4100–4108.

McHale, M. K., G. F. Hall, and M. J. Cohen. 1995. Early cytoskeletal changes following injury of giant spinal axons in the lamprey. *J. Comp. Neurol.* 353:25–37.

Mewis, J., W. J. Frith, T. A. Strivens, and W. B. Russel. 1989. The rheology of suspensions containing polymerically stabilized particles. *AIChE J.* 35:415–422.

Milner, S. T., T. A. Witten, and M. E. Cates. 1988. Theory of the grafted polymer brush. *Macromolecules.* 21:2610–2619.

Mukhopadhyay, R., and J. H. Hoh. 2001. AFM force measurements on microtubule-associated proteins: the projection domain exerts a long-range repulsive force. *FEBS Lett.* 505:374–378.

Mullins, R. D., J. F. Kelleher, J. Xu, and T. D. Pollard. 1998. Arp2/3 complex from acantamoeba binds profilin and cross-links actin filaments. *Mol. Biol. Cell.* 9:841–852.

Nixon, R. A., P. A. Paskevich, R. K. Sihag, and C. Y. Thayer. 1994. Phosphorylation on carboxyl-terminus domains of neurofilament proteins in retinal ganglion-cell neurons in-vivo—influences on regional neurofilament accumulation, interneurofilament spacing, and axon caliber. *J. Cell Biol.* 126:1031–1046.

Pearson, L. T., S. I. Chan, B. A. Lewis, and D. M. Engelman. 1983. Pair distribution-functions of bacteriorhodopsin and rhodopsin in model bilayers. *Biophys. J.* 43:167–174.

Perelson, A. S. 1978. Spatial-distribution of surface-immunoglobulin on B lymphocytes—local ordering. *Exp. Cell Res.* 112:309–321.

Pincus, P. 1991. Colloid stabilization with grafted polyelectrolytes. *Macromolecules.* 24:2912–2919.

Povlishock, J. T., and C. W. Christman. 1995. The pathobiology of traumatically induced axonal injury in animals and humans—a review of current thoughts. *J. Neurotrauma.* 12:555–564.

Pusztai, L., and G. Toth. 1991. On the uniqueness of the reverse Monte-Carlo simulation.1. Simple liquids, partial radial-distribution functions. *J. Chem. Phys.* 94:3042–3049.

Romero, P., Z. Obradovic, C. R. Kissinger, J. E. Villafranca, E. Garner, S. Guilliot, and A. K. Dunker. 1998. Thousands of proteins likely to have long disordered regions. *Pacific Symp. Biocomput.* 3:437–448.

Romero, P., Z. Obradovic, X. Li, E. C. Garner, C. J. Brown, and A. K. Dunker. 2001. Sequence complexity of disordered proteins. *Proteins Struct. Funct. Genet.* 42:38–48.

Rost, B., and C. Sander. 1993. Prediction of protein secondary structure at better than 70-percent accuracy. *J. Mol. Biol.* 232:584–599.

Rost, B., and C. Sander. 1994. Combining evolutionary information and neural networks to predict protein secondary structure. *Proteins Struct. Funct. Genet.* 19:55–72.

Rout, M. P., J. D. Aitchison, A. Suprapto, K. Hjertaas, Y. Zhao, and B. T. Chait. 2000. The yeast nuclear pore complex: composition, architecture, and transport mechanism. *J. Cell Biol.* 148:635–652.

Smith, D. H., J. A. Wolf, T. A. Lusardi, V. M. Y. Lee, and D. F. Meaney. 1999. High tolerance and delayed elastic response of cultured axons to dynamic stretch injury. *J. Neurosci.* 19:4263–4269.

Strong, M. J., W. L. Strong, H. Jaffe, B. Traggert, M. M. Sopper, and H. C. Pant. 2001. Phosphorylation state of the native high-molecular-weight neurofilament subunit protein from cervical spinal cord in sporadic amyotrophic lateral sclerosis. *J. Neurochem.* 76:1315–1325.

Tamashiro, M. N., E. Hernandez-Zapata, P. A. Schorr, M. Balastre, M. Tirrell, and P. Pincus. 2001. Salt dependence of compression normal forces of quenched polyelectrolyte brushes. *J. Chem. Phys.* 115: 1960–1969.

Toth, G., and A. Baranyai. 1997. Conceptual and technical improvement of the reverse Monte Carlo algorithm. *J. Chem. Phys.* 107:7402–7408.

Uversky, V. N., J. R. Gillespie, and A. L. Fink. 2000. Why are "natively unfolded" proteins unstructured under physiologic conditions? *Proteins Struct. Funct. Genet.* 41:415–427.

Willard, M., and C. Simon. 1981. Antibody decoration of neurofilaments. *J. Cell Biol.* 89:198–205.

Wootton, J. C., and S. Federhen. 1996. Analysis of compositionally biased regions in sequence databases. *Methods Enzymol.* 266:554–571.

Yang, Y. M., J. Dowling, Q. C. Yu, P. Kouklis, D. W. Cleveland, and E. Fuchs. 1996. An essential cytoskeletal linker protein connecting actin microfilaments to intermediate filaments. *Cell.* 86:655–665.

Yin, X. H., T. O. Crawford, J. W. Griffin, P. H. Tu, V. M. Y. Lee, C. M. Li, J. Roder, and B. D. Trapp. 1998. Myelin-associated glycoprotein is a myelin signal that modulates the caliber of myelinated axons. *J. Neurosci.* 18:1953–1962.

Zilman, A. G., and S. A. Safran. 2001. Entropically driven attraction between telechelic brushes. *Eur. Phys. J. E.* 4:467–473.